ELSEVIER

Journal of Fluids and Structures 20 (2005) 589–609

JOURNAL OF FLUIDS AND STRUCTURES

www.elsevier.com/locate/jfs

# A finite cantilevered cylinder in a cross-flow

Y. Liu*, R.M.C. So, Z.X. Cui

*Department of Mechanical Engineering, The Hong Kong Polytechnic University, Hung Hom, Kowloon, Hong Kong*

Received 20 September 2004; accepted 20 February 2005

**Abstract**

Numerous factors contribute to the three-dimensional behavior of the wake behind a finite cylinder with relatively large aspect ratio in a cross flow; among the more important ones are the trailing vortex shed from the free end and the necklace vortex formed at the cylinder base. The trailing vortex interacts strongly with the flow around the cylinder; thus giving rise to oblique vortex shedding and changes the flow structures, such as the vortex pattern, and the pressure distribution around the cylinder. Formation of a necklace vortex near the base of the cylinder could give rise to interaction between this vortex and the shed vortices along the cylinder span. Besides, the necklace vortex could even interact with the trailing vortex, depending on the cylinder aspect ratio. For aspect ratios greater than a critical value a suppressed two-dimensional region exists with vortex shedding resembling the Karman vortex street. In this paper, a lattice Boltzmann method is used to numerically simulate the flow past a finite cylinder with an aspect ratio of 10 at Reynolds numbers (Re) varying from 100 to 200. A major finding is that, even in this limited Re range, the wake behavior and flow-induced forces are greatly affected by Re. A suppressed two-dimensional region exists but its size decreases as Re increases. In addition, the effects of the trailing and necklace vortices on the variation of the Strouhal number, and the mean and root mean square drag and lift coefficients along the span are found to be affected by Re.


*Keywords:* Cantilevered cylinder; 3-D effects; LBM

## 1. Introduction

The flow around a two-dimensional (2-D) circular cylinder with finite aspect ratio ($L/D$) has been investigated extensively in the past because it is associated with some complex physical phenomena and because of its intrinsic importance to civil and wind engineering applications; here, $L$ is the span and $D$ is the diameter of the cylinder. Among the major features investigated are the wake characteristics and the vortex street, and the effects of such factors as Reynolds number, free-stream turbulence, $L/D$, surface smoothness, etc., on the wake behavior and on the vortex patterns and their stability. Some major findings are the nature of the wake and its dependence on the Reynolds number ($\mathrm{Re} = U_\infty D/\nu$), where $U_\infty$ is the free-stream velocity and $\nu$ is the fluid kinematic viscosity. For example, the wake was found to be laminar and 2-D at $\mathrm{Re} = 100$ (Zhang and Dalton, 1998), and 3-D and turbulent for $\mathrm{Re} > 400$ (Bloor, 1964).

The 3-D nature of the wake flow was found to consist of such behavior as oblique and parallel vortex shedding patterns (Williamson, 1989), cellular shedding and associated vortex dislocations (Eisenlohr and Eckelmann, 1989; Kŏng et al., 1990; Williamson, 1992), and different instability modes (Williamson, 1988, 1996a). The boundary

*Corresponding author. Tel.: +852 2766 7814; fax: +852 2365 4703.
*E-mail address:* mmyliu@polyu.edu.hk (Y. Liu).

0889-9746/$ - see front matter 
doi:10.1016/j.jfluidstructs.2005.02.009

conditions at the cylinder ends were found to affect the vortex shedding pattern (Berger and Willie, 1972) and to depend on whether the ends were free or equipped with end plates (Gerich and Eckelmann, 1982; Szepessy and Bearman, 1992). The affected region is Re-dependent (Slaouti and Gerrard, 1981; Stager and Eckelmann, 1991). Comprehensive reviews of recent advances and bluff body wakes are given by Roshko (1993), Williamson (1996b), Zdravkovich (1997), and Matsumoto (1999). Besides these studies on the wake and the vortex shedding patterns and stability, numerous investigations have also been carried out on the unsteady induced forces acting on the cylinder. Various methods of measuring the forces have been used and these included direct as well as indirect methods. A comprehensive analysis of the experimental and computational force coefficient results is given by Norberg (2003).

All these studies are concerned with finite (2-D) cylinder where the span extends the entire width (height) of the wind tunnel test-section; i.e., the finite cylinder is not mounted as a cantilever. A finite cylinder with a free end mounted as a cantilever gives rise to additional complication compared to the 2-D cylinder case and can be seen as the simplified geometry of many civil engineering structures and tall buildings. Two complications could be identified as a result of the free end and the extent of these effects will depend greatly on Re and $L/D$. These complicating effects are caused by the free end and by the base flow around the cylinder. The flow separates from the top of the cylinder to form a trailing vortex, and this will interact with the shed vortices from the cylinder surface, depending on $L/D$. If the cylinder is longer than the critical length for Karman vortex shedding to take place, an oblique vortex shedding pattern will result (Kawamura et al., 1984). This is an indication of the interaction between the trailing and shed vortices. The root of the cylinder is usually embedded in the wall boundary layer. Therefore, in the base region, a necklace (horseshoe) vortex will form. This rather general behavior is observed for cylinders with circular as well as square cross-section and with different free-end shapes (Sakamoto and Arie, 1983; Okamoto and Sunabashiri, 1992; Park and Lee, 2000, 2004; Martinuzzi and Tropea, 1993). The behavior is highly dependent on $L/D$ though; e.g., as $L/D$ is decreased to 2 or less, the vortex shedding region, known as a suppressed 2-D vortex shedding region, would disappear (Kawamura et al., 1984). A recent LES simulation of the flow around a finite cylinder with $L/D = 2.5$ revealed that the average flow exhibited an arch-type vortex behind the cylinder (Fröhlich and Rodi, 2004), much like that observed in the flow around a wall-mounted cube (Martinuzzi and Tropea, 1993). These results are consistent with the observations of Kawamura et al. (1984).

The effect of the trailing vortex and wake flow on the unsteady flow-induced forces has been investigated experimentally by Farivar (1981), who carried out measurements over an aspect ratio range of $1 \leqslant L/D \leqslant 40$ at $\mathrm{Re} = 7 \times 10^4$. Similar experiments have also been carried out by Sakamoto and Oiwake (1984). Farivar's (1981) results showed that the mean drag coefficient $C_D$ decreased as $L/D$ decreased. This could be due to the fact that the trailing vortex effect was only confined to a region near the free end, and a suppressed 2-D flow exists in the lower part of the cylinder (Kawamura et al., 1984). As $L/D$ decreased, the suppressed 2-D flow region also decreased and eventually disappeared. Experiments by Fox and West (1993) indicated that the effect of the free-end disturbance was confined within $20D$ from the free-end. Three distinct sets of vortex rows with different frequencies were measured by Farivar (1981), thus giving rise to three different Strouhal numbers ($\mathrm{St} = \Omega_s D/U_\infty$) along the span; here, $\Omega_s$ is the shedding frequency.

A direct force cell measurement technique has been put forward by Richter and Naudascher (1976) to measure the spanwise average unsteady forces in a laminar flow. This technique was extended to measure the unsteady forces in a turbulent stream (So and Savkar, 1981) in an attempt to study the buffetting effect on the unsteady forces. The technique was further extended to measure the local unsteady forces by Sin and So (1987). Baban et al. (1989) applied this technique to measure the local unsteady forces directly along the span of a finite cylinder ($L/D = 2$) and showed, for the first time, that the fluctuating drag was larger than the fluctuating lift and that the characteristic frequency was larger than the vortex shedding frequency. A detailed investigation of the local unsteady forces and wake flow was carried out by Baban and So (1991a) where the correlations between the unsteady forces and the wake velocity were measured. For cylinders with $L/D \leqslant 2$, they showed that the recirculating flow behind the cylinder was responsible for the fluctuating drag. The trailing and necklace vortices shed from the cylinder gave rise to a fluctuating lift that was smaller than the fluctuating drag. In fact, the root-mean-square (r.m.s.) drag coefficient $C'_D$ was more than two times larger than the r.m.s. lift coefficient $C'_L$.

The effects of $L/D$ on $C_D$ and $C'_D$ were further examined by Baban and So (1991b). Even though they have only examined three values of $L/D$, their results clearly showed that $C_D$ increased with $L/D$. Their results were consistent with the investigations of Sarode et al. (1981) and Okamoto et al. (1992) who reported that the overall $C_D$ increased with $L/D$. Baban and So (1991b) further showed that $C_D$ and $C'_D$ increased from cylinder root to a maximum along the span and then decreased toward the free end. The location of the maximum tended to move toward the free end as $L/D$ increased. This trend was in agreement with the spanwise pressure distribution measurements reported by Farivar (1981). On the other hand, $C'_L$ increased as the root of the cylinder was approached and the trend was opposite to that of $C'_D$. All the above investigations were conducted at $\mathrm{Re} \sim 10^4$; in much lower Re range, the number of studies is small. Dauchy et al. (1997) numerically and theoretically investigated the primary and secondary instabilities in the laminar

wake (Re $<100$) and indicated that the recirculation around the cylinder free end was basically responsible for the onset of the secondary instability.

From this brief review, it is obvious that the flow and unsteady forces acting on a finite cylinder at low Re has only been investigated sparingly. The effect of the free end on the wake flow and the unsteady forces has not been studied systematically. Among the more important features are the effect of Re on the wake flow, the separate interaction effect of the trailing and necklace vortices with the shed vortices from the cylinder, and their combined effect on the flow-induced forces. Therefore, the objectives of this study are to explore these various effects at a fixed $L/D$ for three Re. A value of $L/D = 10$ is chosen, so that a suppressed 2-D region still exists along the span of the cylinder. The reason for this choice of $L/D$ will be made clear later. In particular, the study examines the nature of vortex shedding, the effect of the trailing vortex on shedding, and the behavior of St, $C_D$, $C'_D$ and $C'_L$ along the span of the cylinder.

## 2. Numerical method

Numerical simulation is used to analyze the problem of a finite cantilevered cylinder in a cross-flow. The choice of the numerical method is the lattice Boltzmann method (LBM) where the lattice Boltzmann equation (LBE) is solved instead of the Navier–Stokes equation. It should be pointed out that, if the solution of the LBE is to recover the incompressible Navier–Stokes equation correctly, the Mach number ($M$) effect on the density fluctuation of existing LBM should be minimized. This is accomplished through a combination of the application of the Chapman–Enskog procedure and a numerical method to minimize the $M$ effect in the solution of the LBE (McNamara and Zanetti, 1988; Chen et al., 1992; He and Luo, 1997a; Guo et al., 2000; Yu et al., 2002). It is in this sense that the LBM is used to resolve the incompressible flow field in the present problem. The reason for this choice is because a recent study on 3-D incompressible flow behind a nominally 2-D cylinder showed that the method gives credible results for the wake flow and unsteady forces (So et al., 2005).

A schematic view of the problem and the computational domain is shown in Fig. 1. The cylinder with $L/D = 10$ is mounted as a cantilever with a free end exposed to the cross-flow. The upper and lower walls of the test-section are set to give no-slip boundary condition. Incompressible flow with constant fluid density $\rho$ and constant dynamic viscosity $\mu$ is assumed. A Cartesian coordinate system $(x,y,z)$, where the $x$-axis is aligned with the incoming flow direction (streamwise direction), the $y$-axis is perpendicular to the plane containing the streamwise and spanwise direction ($z$-axis) is used to describe the flow. The $z$-axis is chosen to coincide with the cylinder axis. Hence, the origin of the coordinate system is placed on this axis, with $z = 0$ located at the base of the cylinder. All coordinates are normalized by $D$ and the physical parameters by $D$, $\rho$, $\mu$ and $U_\infty$, such that $X = x/D$, $Y = y/D$ and $Z = z/D$. The normalized flow-induced force coefficient acting on the cylinder axis is decomposed into a drag coefficient $C_D(0,0,Z,t)$ and a lift coefficient $C_L(0,0,Z,t)$, where the nondimensional time is defined as $t = \tilde{t}U_\infty/D$ and the nondimensional velocity vector and static pressure defined as $\mathbf{u} = \tilde{\mathbf{u}}/U_\infty$ and $p = \tilde{p}/\rho U_\infty^2$. Here, a tilde is used to denote dimensional quantities and a bold face used to denote vector quantities.

### 2.1. Lattice Boltzmann method

The lattice Boltzmann method (LBM) has been used by many to carry out incompressible flow calculations recently; therefore, the technique is well accepted. In LBM, the convection operator (or streaming process) in phase space (or

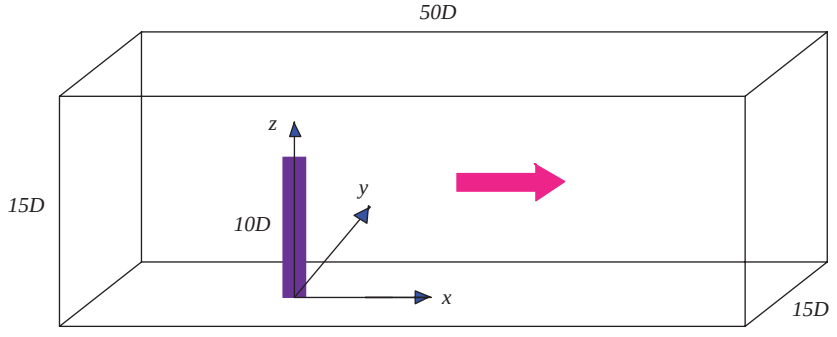


Fig. 1. Schematic view of the problem.

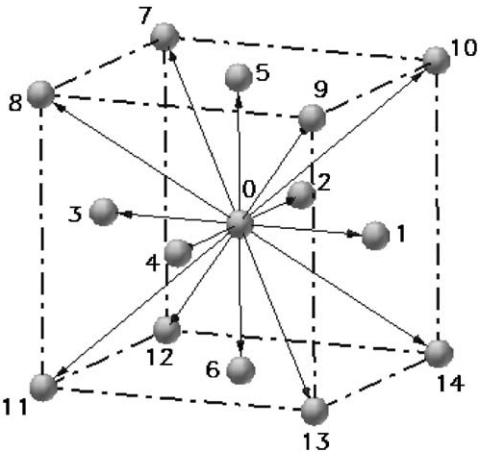


Fig. 2. Schematic representation of the D3Q15 model.

velocity space) is linear. This feature is borrowed from kinetic theory and contrasts with the nonlinear convection terms in other approaches that use a macroscopic representation. Simple convection combined with a relaxation process (or collision operator) allows the recovery of the nonlinear macroscopic advection through multi-scale expansions. Therefore, the incompressible Navier–Stokes equation can be recovered correctly from the Boltzmann equation using the BGK collision operator (Bhatnagar et al., 1954), the Chapman–Enskop procedure and a technique to eliminate terms of order $M^2$ due to the density fluctuation in existing LBM. The equation with the BGK collision operator substituted can be written as

$$\frac{\partial f}{\partial t} + \mathbf{e} \cdot \nabla f = -\frac{f - f^{\mathrm{eq}}}{\lambda}, \tag{1}$$

where $\lambda$ is the relaxation time due to particle collision, $f$ is the particle distribution function and $f^{\mathrm{eq}}$ is the equilibrium Boltzmann–Maxwell distribution function. It can be shown that the particle velocity field $\mathbf{e}$ can be discretized using a small set of vectors $\{\mathbf{e}_i\}$ such that the macroscopic conservation laws are satisfied (He and Luo, 1997b). The Boltzmann equation (1) can be discretized along each velocity direction $\mathbf{e}_i$ at each lattice. The result is commonly called the lattice BGK model which is solved assuming a $D_3Q_{15}$ velocity model (Fig. 2). Other velocity models have been tested, but the results were not as satisfactory compared to the $D_3Q_{15}$ model. The formulation and solution procedure follows closely that presented in So et al. (2005). In view of this, there is no need to repeat the details of the LBM again. Details of the method could be found in Cercignani (1988), Guo et al. (2000), So et al. (2005) and other references given in these papers.

### 2.2. Boundary conditions and mesh refinement

Unlike Navier–Stokes solvers, the basic evolution variable in the LBM is $f$, which is usually not specified at the boundaries. Therefore, when the macroscopic variable distributions at the boundary are known, it is important to find an appropriate particle distribution such that it can meet the specified boundary condition. The current non-equilibrium extrapolation treatment is based on the decomposition of the distribution function and still gives second-order accuracy without having to make additional assumptions. The details of the boundary treatment has been discussed elsewhere (So et al., 2005).

In the present problem, the vortices shed from the cylinder form a vortex street behind the cylinder. If the vortex street is to be developed fully, the downstream computation domain has to be long enough. Furthermore, accurate resolution of the boundary layer developed around the cylinder surface is important for the calculation of the development of the vortex street. Therefore, a mesh refinement technique is adopted to accommodate the high gradient in the velocity boundary layer around the cylinder. The computational domain is specified as $50 \times 15 \times 15$ in the $X$, $Y$ and $Z$ direction, respectively, with the inlet located at $X = -10$ and the $Y$-axis extends from $-7.5$ to 7.5. A coarse grid given by $D/8$ is defined for the whole flow field. Around the cylinder, a fine mesh region measured $6 \times 4 \times 11.5$ is specified. The upstream boundary of this fine mesh is located at $X = -2$ and the fine mesh is defined by $D/24$. On the coarse–fine mesh interface, the macroscopic variables and their derivatives are required to be continuous. Another fine

mesh defined by $D/32$ has also been used to perform the calculations at $Re = 100$. Results showed that the calculations obtained from these two fine grids differ only by 1% or less. Subsequently, all calculations were carried out using the fine grid specified by $D/24$. Details of the mesh refinement technique are given in So et al. (2005).

### 2.3. Data analysis

If the time series given by the LBM simulation were stationary, they can be analyzed using a fast Fourier transform (FFT) technique. For 2-D and 3-D wake flow behind a cylinder, the velocity, pressure, and lift and drag signals are essentially stationary. However, for 3-D flow behind a 2-D cylinder, the drag signal is non-stationary (So et al., 2005). For the present problem, the interaction between the trailing and necklace vortex with the flow around the cylinder could render the lift and drag signals non-stationary. In view of this, the calculated time series signals of lift, drag, etc. are checked for stationarity using the wavelet analysis technique to analyze the localized variation of power within a time series. This technique has been outlined in So et al. (2005); it will not be repeated here.

## 3. Results and discussion

The rationale for the choice of parameters investigated will now be made clear. From the studies of Farivar (1981), Kawamura et al. (1984), Baban and So (1991b) and Fröhlich and Rodi (2004), it is known that the wake flow and induced unsteady forces on the finite cylinder are greatly dependent on $L/D$ for a given Re. In the Re range investigated by the above researchers, i.e. $Re > 10^4$, a suppressed 2-D region was found to exist when $L/D > 6$ and this region completely disappeared when $L/D \leqslant 2.5$. That is, the suppressed 2-D region slowly disappeared between $2.5 < L/D < 6.0$. It is also known that for a given $L/D$, the suppressed 2-D region would depend on Re, although the extent of this dependence is not known. Furthermore, for given Re and $L/D$, the wake flow behavior and unsteady forces will also be influenced by turbulence in the free stream (which affects the separation behavior from the free end), transition to turbulence in the wake and a fully turbulent wake. Most of the investigations reviewed in the Introduction were carried out at $Re > 10^4$. At this Re, the wake is fully turbulent. If the dependence on Re were to be investigated, it would be better to isolate other effects such as free-stream turbulence. In view of this, the present choice of very low Re at a fixed $L/D$ would allow the effect of Re on the wake flow and unsteady forces to be investigated thoroughly. It would also permit the effect of the interaction of the trailing and necklace vortices with the flow around the cylinder to be examined, together with the extent of these interactions on the suppressed 2-D region. Consequently, $L/D = 10$, and $Re = 100$, 150 and 200 are selected. A secondary reason for these choices of Re and $L/D$ is that the LBM is more reliable at low than at high Re. The recent study by So et al. (2005) showed that the LBM gave reliable results for the calculation of 3-D flow and unsteady forces on a nominally 2-D cylinder.

For the cantilevered cylinder, the trailing vortex (or separated flow) emanating from the free end and vortices shed from the cylinder surface would interact to change the flow structure significantly in the near wake. Besides this interaction, a necklace vortex would also form near the base of the cylinder, and this too would interact with the shed vortices from the cylinder surface. These interactions near the free end and the base would greatly affect the shed vortex behavior and subsequently the flow-induced unsteady forces acting on the cylinder. The extent of these interactions on the unsteady forces is not known unless and until their effects on the wake flow are understood. This study aims to seek understanding of the effects of these interactions on the unsteady forces. Therefore, in the following, the wake flow is examined first. A fairly detailed analysis of the unsteady force behavior along the span of the finite cylinder and the influence of the wake flow on the unsteady forces is then presented.

### 3.1. Wake flow behavior

There are many ways to examine the wake flow behavior. In the present study, the vorticity distribution behind the cylinder for the three Re values calculated will be analyzed in detail. These plots will be supplemented by flow-vector plots and flow visualization if necessary, to illustrate the effect of Re on the suppressed 2-D region and on the extent of the interactions between the trailing and necklace vortices with the flow around the cylinder. The calculations of the two components of vorticity, $\boldsymbol{\varpi}_y$ and $\boldsymbol{\varpi}_z$, and the flow vectors from the LBM simulations are quite standard; therefore, there is no need to repeat how these calculations are performed here. The vorticity component $\boldsymbol{\varpi}_x$ would not help shed light on the wake behavior; consequently, its distribution in the near wake is not examined. Flow visualization experiments were performed to verify the calculated physics of the near-wake flow for the case $Re = 100$. They were carried out in the same water tunnel using an identical LIF technique as that employed by Lam et al. (2004) to study the 3-D wake

vortices in the near wake of a wavy cylinder. The flow visualization experiment gives the development of the flow pattern because the video camera captures the movement of the dye ejected from the cylinder and illuminated by the laser. Details of the water tunnel set-up and the LIF technique are described in Lam et al. (2004); interested readers are referred to their study.

The distributions of $\varpi_z$ in the $X-Y$ plane behind the cylinder at Re = 100, 150 and 200 are plotted in Figs. 3(a)–(c), for comparison. The region covers $-2 \leqslant X \leqslant 32$ and $-7 \leqslant Y \leqslant 7$. In each figure, the $\varpi_z$ at five different $Z$ locations are shown. These $Z$ locations are selected to display the vorticity behavior at the center as well as near both ends; consequently, they are chosen at $Z = 1$ (near the base), 3, 5, 7 and 9 (near the free end). At $Z = 9$, no vortex shedding can be clearly identified, thus indicating that vortex shedding from cylinder surface is suppressed by the trailing vortex emanating from the free end of the cantilevered cylinder. The vorticity distribution strongly suggests that the near-wake flow is very similar to that observed for 2-D cylinder with very low Re; i.e., a closed recirculation region with two symmetric vortices is formed behind the cylinder. This is clearly illustrated by the flow-vector plot shown in Fig. 4 at $Z = 9$ for the region covering $-2 \leqslant X \leqslant 4$ and $-2 \leqslant Y \leqslant 2$. In Fig. 4, the flow pattern results from the visualization experiment are also displayed alongside the vorticity and flow-vector plots. This result is consistent with the vorticity and flow-vector plots.

At $Z = 7$, the free end effect is not as strong; consequently, alternating vortices are shed from the cylinder surface. However, the resultant $\varpi_z$ is very weak. At mid-plane ($Z = 5$), vortex shedding is much stronger and it clearly shows a Karman vortex street. The vortex pattern resembles a 2S pattern. Referring to Fig. 4, the flow-vector plot and the flow pattern deduced from the visualization experiment essentially substantiate this interpretation. The 2S vortex pattern is clearly visible from the flow visualization experiment as well as from the flow-vector plot. As the base is approached ($Z = 3$), the shed vortices increase in strength, and it appears that a "P" type vortex pattern starts to emerge. It seems that the vortex pattern is undergoing a transition from a 2S type to a 2P type. At $Z = 1$, vortex shedding is again suppressed due to the interference of the necklace vortex on the shed vortices, thus changing the behavior of $\varpi_z$ completely. The result of this interaction is very similar to that observed near the free end. However, the effect is not as strong. An examination of the flow-vector plot and the flow visualization result shown in Fig. 4 at $Z = 1$ essentially verifies the above interpretation. There is one difference in the flow-vector plots at $Z = 1$ and 9 though. The closed region behind the cylinder is longer at $Z = 1$ and there is only one vortex within the closed region. This points to the fact that the interaction effect near the base is different from that near the free end. The difference could affect the development of the unsteady forces on the cylinder.

Corresponding $\varpi_z$ results for Re = 150 and 200 are shown in Figs. 3(b) and (c), respectively. The overall behavior is very similar to that shown for Re = 100. There are minor differences and these are pointed out below. As Re increases, the interaction of the trailing vortex with the shed vortices gives rise to slightly different shedding behavior at $Z = 7$, but essentially the same at $Z = 9$. The alternating behavior at Re = 100 begins to disappear as Re increases and is quite evident at Re = 200. Another difference is the vortex shedding pattern at $Z = 5$. The pattern is 2S at Re = 100, begining to undergo transition to a 2P pattern as Re increases, completely becomes a 2P pattern at Re = 200. The same trend is also observed at $Z = 3$. At this $Z$ location, the transition to a 2P pattern actually starts at Re = 100. It assumes a 2P pattern at Re = 150. These differences show that the extent of the interaction between the trailing and necklace vortex with the flow around the cylinder becomes greater as Re increases. The effect of this increase on the development of the unsteady forces will be examined later. The near-wake plots of $\varpi_z$ and the flow vectors are not shown, because they are similar to those given in Fig. 4 for Re = 100.

Having examined the vorticity distributions in the $X$–$Y$ plane, the next step is to investigate the vorticity distributions in the $X$–$Z$ plane. This plane is chosen at $Y = 0$, or the plane that divides the cylinder into two equal halves. Two vorticity components, namely $\varpi_z$ and $\varpi_y$ are calculated. They are plotted in Figs. 5(a)–(c) for the three cases of Re investigated; the case of Re = 100 is shown in Fig. 5(a), Re = 150 in Fig. 5(b) and Re = 200 in Fig. 5(c). In each figure, two panels are shown, the top panel for $\varpi_z$ and the bottom panel for $\varpi_y$. The plots Figs. 5(a)–(c) indicate that $\varpi_z$ is much stronger in the central region behind the cylinder. Near the free end and the base, $\varpi_z$ is very weak. These plots further show that oblique shedding along the cylinder span is clearly visible at Re = 100. As Re increases, the extent of the interaction of the trailing and necklace vortices with the shed vortices becomes greater and greater. At Re = 200, the region where oblique shedding is observed essentially disappears (Fig. 5(c)). Instead, vortex shedding behind the cylinder is no longer organized like that shown in Fig. 5(a).

The bottom panel of Figs. 5(a–c) gives the distribution of $\varpi_y$ and clearly shows the separated flow from the free end of the cylinder. It is obvious that the separated flow does not extend to cover the entire span like the cases investigated by Baban and So (1991a). For these cases where $L/D \leqslant 2$, the separated flow from the free end reattaches to the wall downstream of the cylinder and a recirculation region is formed. This recirculation region completely destroys the spanwise vortex shedding and gives rise to a different behavior for the flow-induced forces. More will be said about this in the next section. There exist pairs of $\varpi_y$ streets behind the cylinder and these pairs of vortex streets converge toward

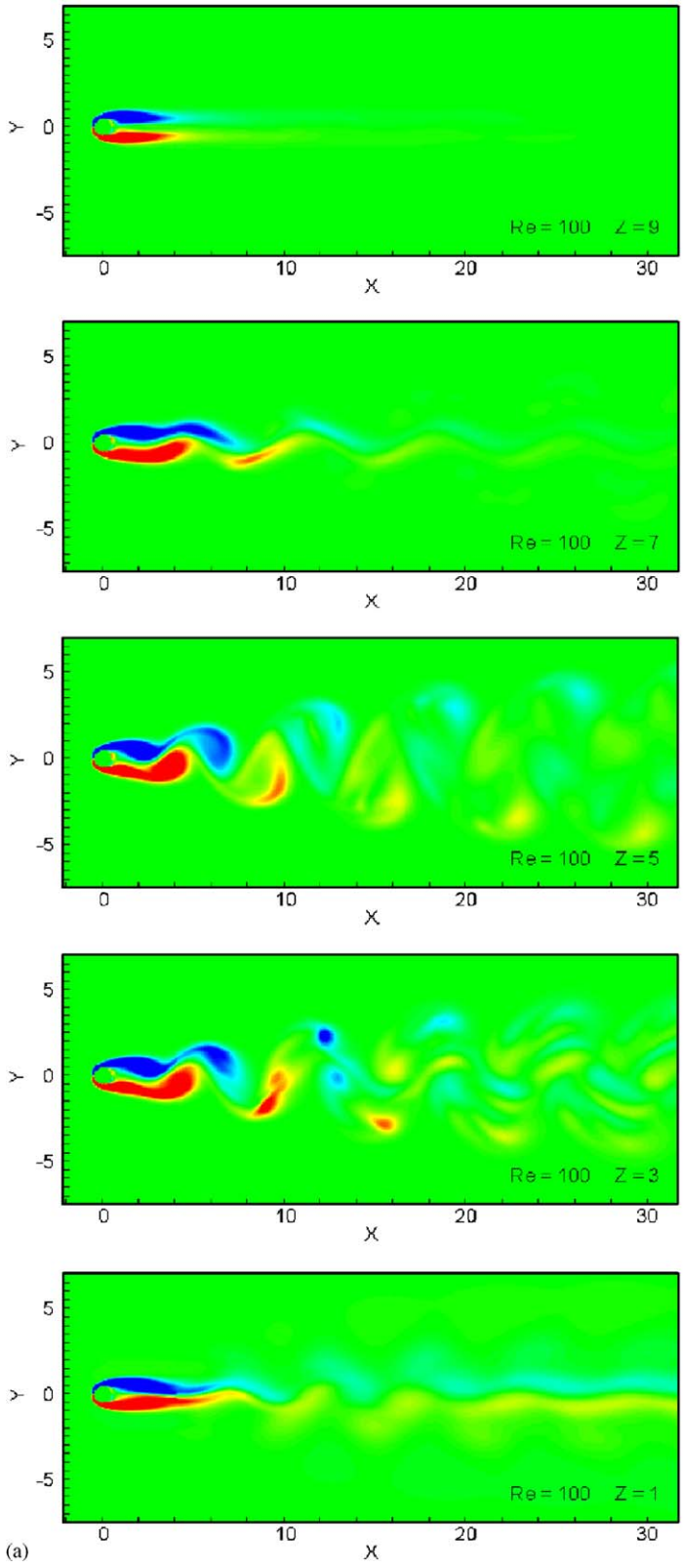


Fig. 3. The vorticity component $\varpi_z$ at different $Z$ locations with (a) Re = 100; (b) Re = 150; (c) Re = 200.

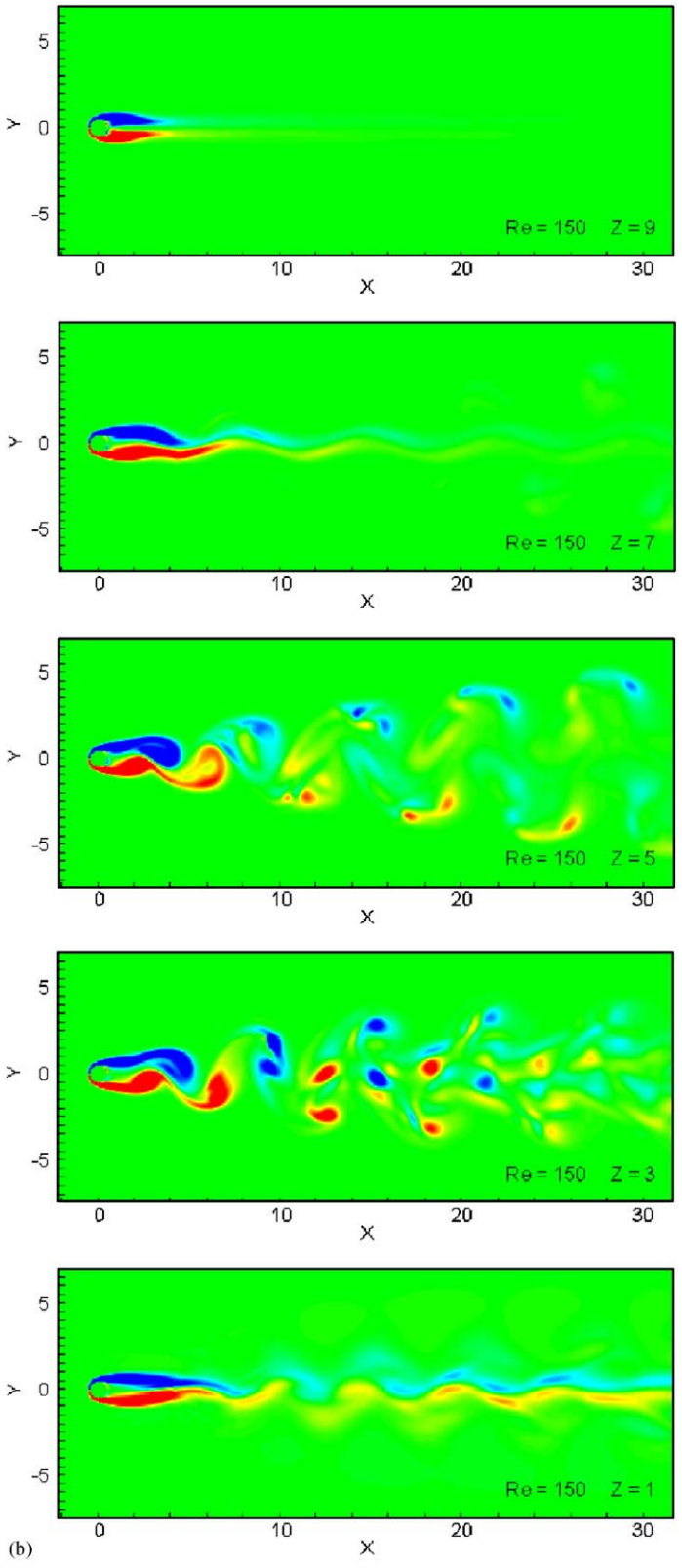


Fig. 3. (*Continued*)

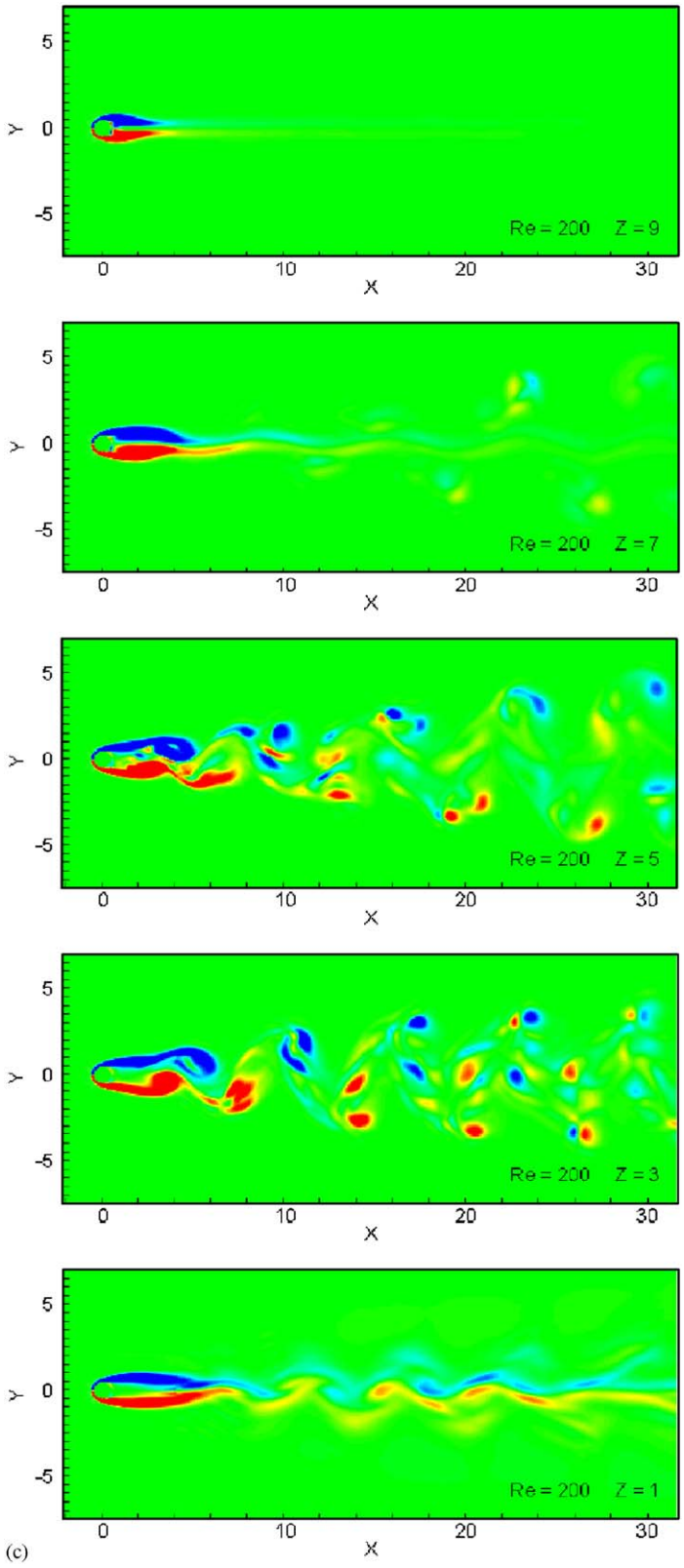


(c)

Fig. 3. (*Continued*)

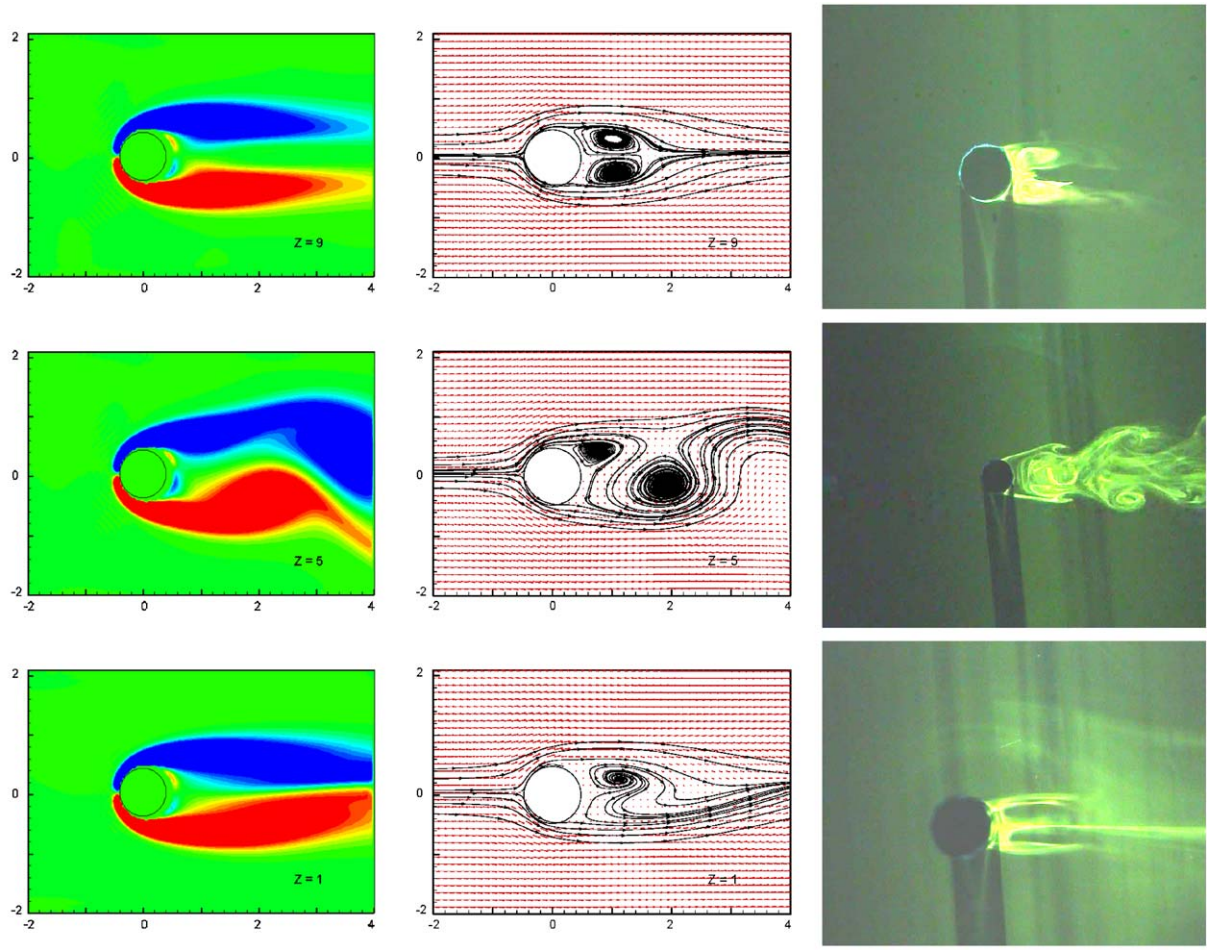


Fig. 4. Enlarged view of $\varpi_z$, flow vectors and visualization for Re = 100 at the $X$–$Y$ plane.

the $Y = 0$ plane far downstream ($X > 30$) of the cylinder. These pairs of vortex streets could be induced by the trailing and necklace vortices emanating from the free end and the base. This overall behavior is observed for all three Re investigated. Of course, Re plays a part in the structure of this $\varpi_y$. An enlarged view of the separated flow region and flow vectors in the $X$–$Z$ plane at Re = 100 together with the visualization result are shown in Fig. 6. It can be seen that the separated shear layer flows down along the cylinder span and it is the interaction of this shear layer with the flow around the cylinder that suppresses vortex shedding ($\varpi_z$) from the cylinder surface. The extent of the penetration could be assessed from the flow-vector plot. It seems that the flow visualization result is quite consistent with the flow-vector plot (Fig. 6).

In summary, these results show that Re has a significant effect on the extent of the interaction at the free end and near the base. This in turn affects the suppressed 2-D region where "normal" vortex shedding is observed. The vortex shedding pattern in this region is dependent on Re and changes from a 2S type to a 2P type as Re increases. In the next section, the effect of these changes on the unsteady forces and their 3-D nature is analyzed and the results are compared with other data whenever available.

### 3.2. Behavior of the unsteady forces

The flow-induced forces can be calculated by either the momentum exchange method or by integrating the pressure distribution around the cylinder at different $Z$ locations. A nice feature of LBM is that the momentum flux tensor is

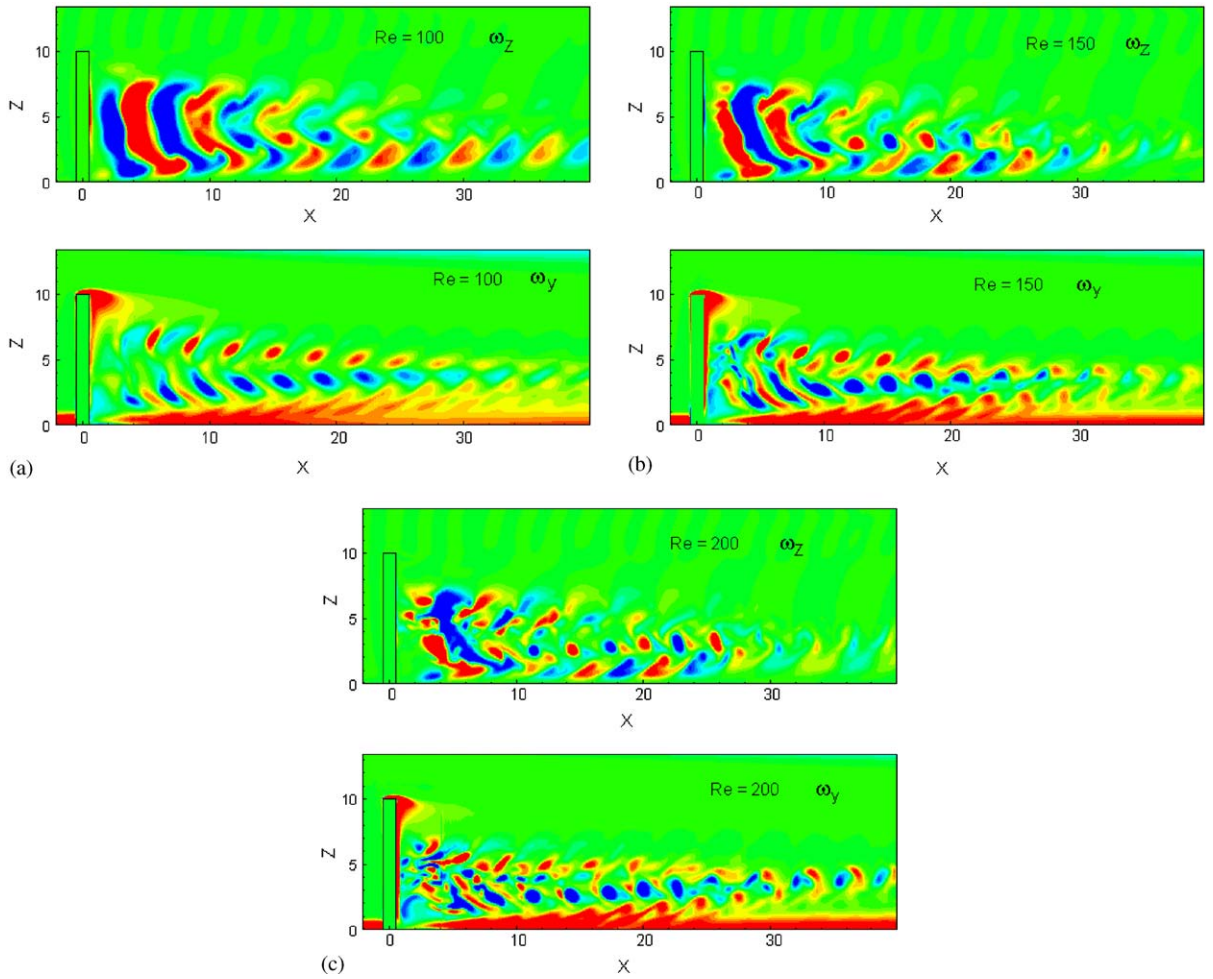


Fig. 5. The vorticity components, $\varpi_z$ and $\varpi_y$, at the $X$–$Z$ plane.

available locally from its very definition. In the present calculation, this method is used to calculate the fow-induced forces. The normalized flow-induced force coefficient acting on the cylinder axis can be decomposed into a drag coefficient $C_D$ (0,0, $Z$,$t$) and a lift coefficient $C_L$ (0,0, $Z$,$t$). From this point on, for the sake of brevity, the drag and lift coefficients are written as $C_D$ ($Z$, $t$) and $C_L$ ($Z$, $t$). The mean and r.m.s. force coefficients can then be calculated from $C_D$ ($Z$, $t$) and $C_L$ ($Z$, $t$) and they are denoted by an overbar and a prime, respectively. For example, the mean drag coefficient is given by $\bar{C}_D$ and the r.m.s. drag coefficient by $C_D'$. In calculating these mean and r.m.s. values, the lift and drag time series are assumed to be stationary; i.e. the mean and r.m.s. values are deduced in a straightforward manner. Verification of this assumption is presented when the spectra of the time series are examined.

Farivar (1981) measured the mean drag coefficient using two different methods: one a direct method that measured the strain, and another by measuring the circumferential pressure distribution at fixed $Z$ locations along the span. The mean drag coefficient thus obtained represents an average over the entire span. No $\bar{C}_D$ was reported. However, the circumferential distributions of the pressure coefficient, $C_p$, at four Z locations for $L/D = 10$ were reported. These results showed that the base pressure is greatly dependent on $Z$; it reaches a minimum as the free end is approached and increases toward the cylinder midspan. This suggests that $\bar{C}_D$ increases from the midspan to the free end of the cylinder. The same trend was also observed by Okamoto and Yagita (1973). These results were obtained at $\mathrm{Re} = 7 \times 10^4$. It would be interesting to compare the present result with that reported by Farivar (1981). The $C_p$ calculated from the surface pressure data at $\mathrm{Re} = 100$ and different $Z$ locations are plotted in Fig. 7. It can be seen that the base pressure follows closely the trend reported by Farivar (1981), indicating an increase in $\bar{C}_D$ as the free end is approached.

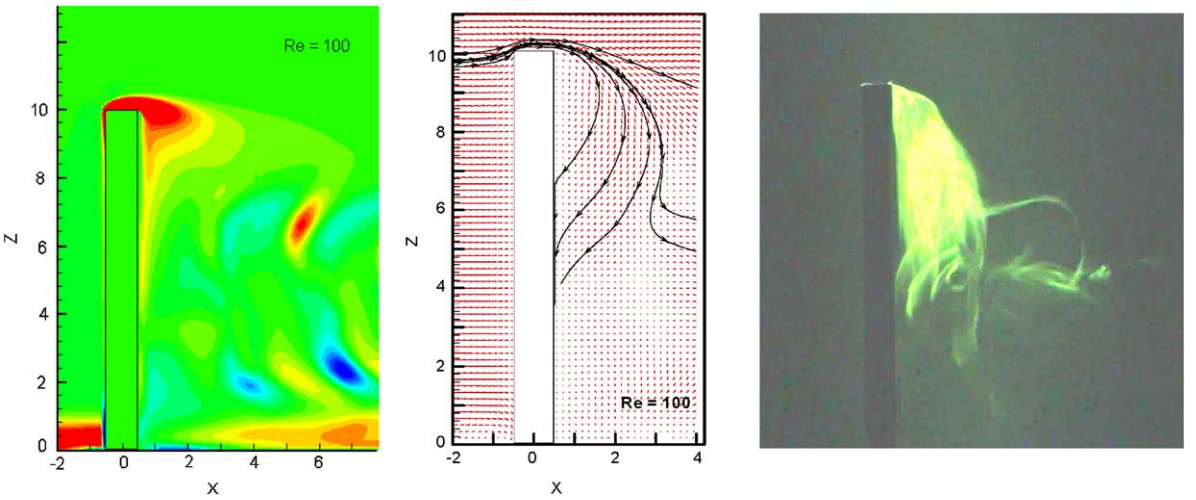


Fig. 6. Enlarged view of $\varpi_y$, flow vectors and visualization for Re = 100 in the $X$–$Z$ plane.

The present results further suggest that $\bar{C}_D$ also increases toward the base. The overall trend is not significantly affected by Re.

The variation of $\bar{C}_D$ along the span with different Re is plotted in Fig. 8. They essentially verify the conclusion drawn from the $C_p$ plots shown in Fig. 7. The trend is similar for all Re investigated. However, there is one difference, and that is the magnitude of $\bar{C}_D$ decreases as Re increases. At mid-span, the reduction amounts to 16% of the value obtained for Re = 100. Since drag is a measure of the momentum deficit in the wake, this implies that the wake is narrower as Re increases. In other words, the interaction of the trailing and necklace vortices has a significant effect on the width of the wake. The growth of the wake at $Z = 5$ and $X = 15$ (or any other $X$ and $Z$ locations) is determined by using the $U_\infty/2$ point to define its width. Thus determined, it is found that the width of the wake is about 27% smaller at Re = 200 compared to that at Re = 100. The increase toward the free end could be due to the effect of the separated region and its interaction with the flow around the cylinder, while the corresponding increase noted near the base is a consequence of the interaction between the necklace vortex and the flow around the cylinder. Near the base, the maximum $\bar{C}_D$ drops as Re increases, but the same is not true near the free end. This tends to suggest that the separated region and its interaction with the flow around the cylinder plays a more important role in the determination of the drag behavior. The fairly constant $\bar{C}_D$ in the central region is a consequence of the existence of the suppressed 2-D region. The reduction in size of this region as Re increases is an indication of the gradual disappearance of the suppressed 2-D region.

The variations of $C'_D$ and $C'_L$ for the three Re investigated are plotted in Figs. 9 and 10, respectively. In order to interpret these results, it is necessary to look into the relation between the $C'_D$ and $C'_L$ data for 2-D and finite cylinders. A recent study by So et al. (2005) on 2-D cylinder with 3-D wake flow at Re = 100 showed that the distributions of $C'_D$ and $C'_L$ are not uniform across the span; however, the ratio of $C'_L/C'_D$ is about 10 at mid-span and varies along the span. The variation is an indication that the unsteady forces are not 2-D. So and Savkar (1981) found that the ratio of the spanwise average force coefficients is also about 10 for the Re range of $10^4 < \mathrm{Re} < 10^5$. As for finite cylinders with $L/D < 2.5$, Baban and So (1991a, b) found that $C'_L/C'_D < 1$. The reason for this is because the recirculation region formed behind the cylinder is responsible for the flow-induced force in the streamwise direction, and there is no visible vortex shedding along the span of the cylinder. As a result, flow-induced lift becomes much less important compared to the induced drag. Depending on $L/D$ and the span location, the ratio could be as small as $\frac{1}{3}$. Their results simply reflect the disappearance of the suppressed 2-D region and the transition to a complete 3-D unsteady force behavior along the span of the finite cylinder. An examination of Figs. 9 and 10 reveals the following. At Re = 100, $C'_D$ is smallest but $C'_L$ is largest. As Re increases, $C'_D$ increases but $C'_L$ decreases. Thus, $C'_L/C'_D$ is largest at Re = 100 among the three Re investigated. This trend follows that shown for the wake behavior; namely that as Re increases the extent of the suppressed 2-D region decreases. Hence, $C'_L$ decreases and $C'_D$ increases with a concomitant decrease of $C'_L/C'_D$. The distribution of $C'_L$ is fairly symmetrical about midspan with its maximum occuring there (Fig. 10). This behavior suggests that the interaction effect on $C'_L$ is about similar at both ends of the cylinder. A minimum $C'_D$ occurs at about $Z = 7$ (Fig. 9). A most likely explanation for this phenomenon is that the shear layer separated from the free end

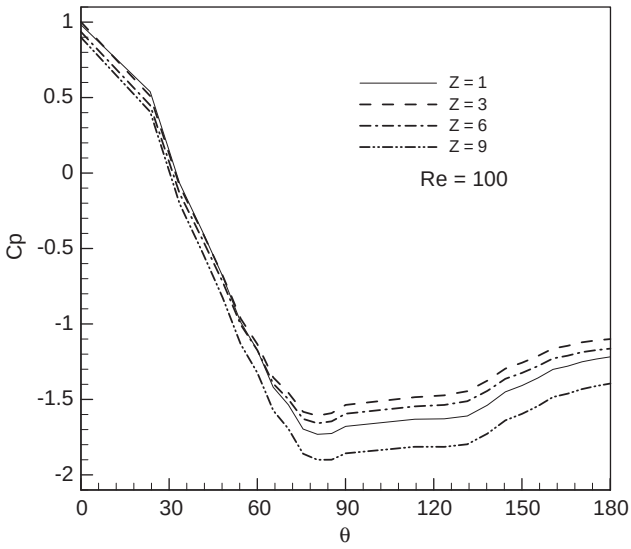


Fig. 7. Circumferential distribution of the pressure coefficient $C_P$ at different $Z$ locations.

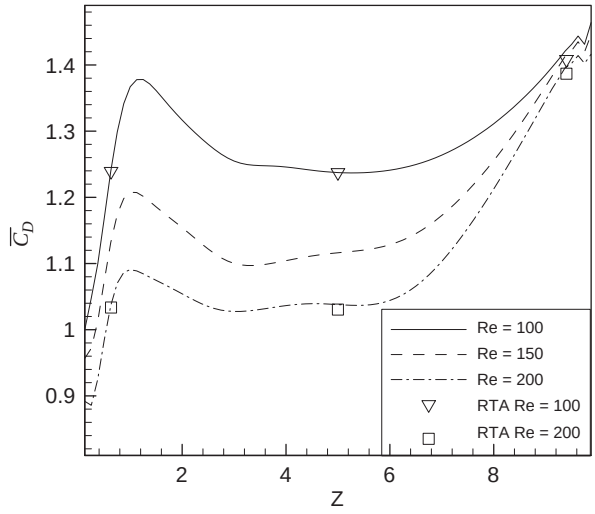


Fig. 8. Spanwise distribution of the mean drag coefficient for different Re.

reverses back toward the cylinder as shown in Fig. 5, and interacts with the separated shear layers from the cylinder at $Z\sim7$. This interaction occurs along the streamwise direction; thus it tends to suppress the oscillation of the streamwise component of the vortex shedding.

### 3.3. Stationary nature of the unsteady forces

The stationary nature of the unsteady forces is further examined. Wavelet analysis is used to analyze the lift and drag time series that might contain non-stationary power at many different frequencies (Daubechies, 1990). By decomposing a time series into time–frequency space, it is possible to determine both the dominant modes of variability and how those modes vary in time. Wavelet analysis has been carried out on the $C_L$ and $C_D$ time series for all Re investigated.

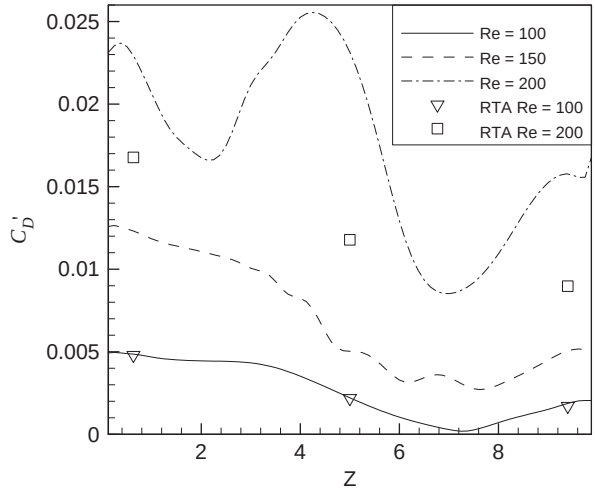


Fig. 9. Spanwise distribution of the r.m.s. drag coefficient for different Re.

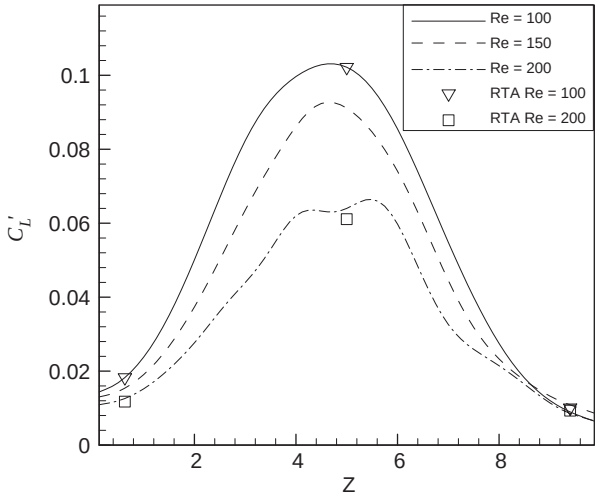


Fig. 10. Spanwise distribution of the r.m.s. lift coefficient for different Re.

Only sample spectral plots at $Z = 9.4$, 5.0 and 0.63 for the $\mathrm{Re} = 100$ case are given in Figs. 11 and 12, and they are shown with St versus $t$. Near the free end and the base, there exist two dominant shedding frequencies, and in midspan the only dominant frequency is $\mathrm{St} = 0.145$ and coincides with one of the St observed elsewhere. The spectral plots show that the $C_L$ time series is indeed stationary because the amplitudes of the St fluctuations do not vary with $t$, consequently, the mean St is essentially constant. The dominant frequency in Fig. 12 is $\mathrm{St} = 0.29$ for all $Z$ locations examined, which is twice that shown for $C_L$. The variation of St in the spectral plots clearly shows that the St envelope and its mean, for all St shown except 0.29, vary with time; thus indicating a non-stationary behavior of the $C_D$ time series. Both the $C_L$ and $C_D$ spectral plots show other dorminant frequencies, besides those characteristic of $C_L$ and $C_D$. Results for other Re are essentially the same; the difference is only in the degree of variation of St with $t$. This analysis, therefore, suggests that the $C_L$ time series is stationary for all Re investigated but the $C_D$ time series is not.

In order to further verify this observation, the mean and r.m.s. values of the unsteady forces are calculated using the running-time-average (RTA) method, which is consistent with the spirit of the continuous wavelet transform (So et al., 2005). A slice of period $2T$ centered around an instantaneous time $t$ is chosen for the determination of the mean and r.m.s. values of the unsteady forces. As the slice is moved along the $t$-axis, the mean and r.m.s. values thus determined

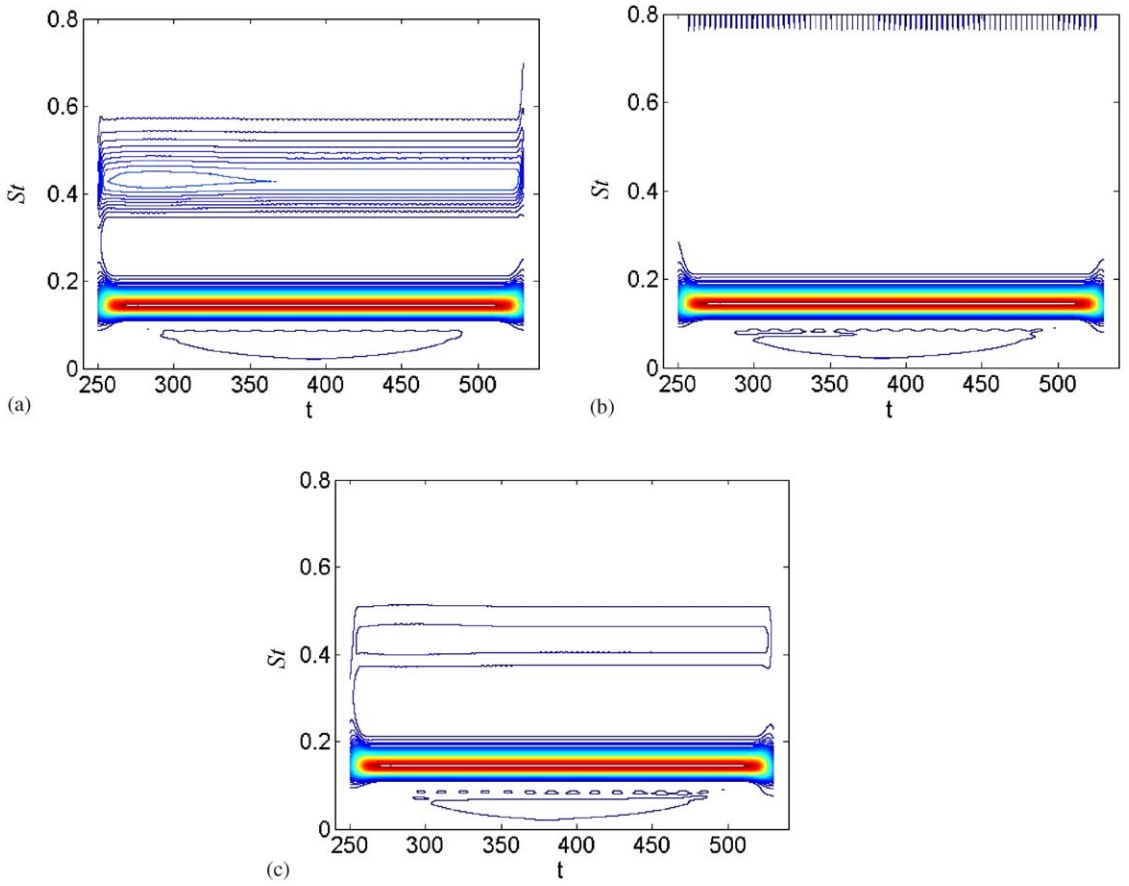


Fig. 11. Wavelet analysis of $C_L$ for (a) $Z = 9.4$, (b) $Z = 5.0$ and (c ) $Z = 0.63$ at $\mathrm{Re} = 100$.

will change with time for non-stationary signals but remain constant if the signals are stationary, provided $2T$ is much larger than the period of the stationary signal. The RTA results for $C'_D$ and $C'_L$ are shown in Fig. 13 for $\mathrm{Re} = 100$ and 200, and three $Z$ locations chosen near the floor, at mid span and near the free end. The time range covered is $260 < t < 490$. It can be seen that the variation of $C'_L$ with $t$ is small; however, the variation is dependent on Re and $Z$. For example, the variation of $C'_L$ is largest for $\mathrm{Re} = 200$ at $Z = 5$. This could be the consequence of the intense mixing of the trailing vortex with shed vortices along the span for this Re in the central region (Figs. 3(c) and 5(c)). The variation of $C'_D$ is very small for $\mathrm{Re} = 100$; however, it becomes quite substantial for $\mathrm{Re} = 200$. This behavior is consistent with the observation for $C'_L$ and could be attributed to the intense mixing between the trailing vortex and the shed vortices along the span. The average at these locations over the $t$ range shown are calculated and plotted in Fig. 9 and 10 for comparison with $C'_D$ and $C'_L$ calculated using the conventional method. In addition, the calculated $\bar{C}_D$ are compared in Fig. 8. The RTA calculated $\bar{C}_D$ and $C'_L$ are in good agreement with the conventionally determined mean and r.m.s. values. As for $C'_D$, the RTA calculated values are in good agreement with the conventionally determined mean and r.m.s. values for the $\mathrm{Re} = 100$ case only. It is not so for the $\mathrm{Re} = 200$ case (Fig. 9). Therefore, this analysis lends credence to the observation that the $C_D$ time series is not stationary for the $\mathrm{Re} = 200$ case, but it is stationary for the $\mathrm{Re} = 100$ case. The $C_L$ time series is essentially stationary for all Re investigated.

### 3.4. Spatial correlation of the unsteady forces

An effective way to examine the three-dimensional nature of the unsteady forces is to calculate the spatial correlation of the forces along the span. From the study of So et al. (2005), it is known that the drag would exhibit 3-D behavior

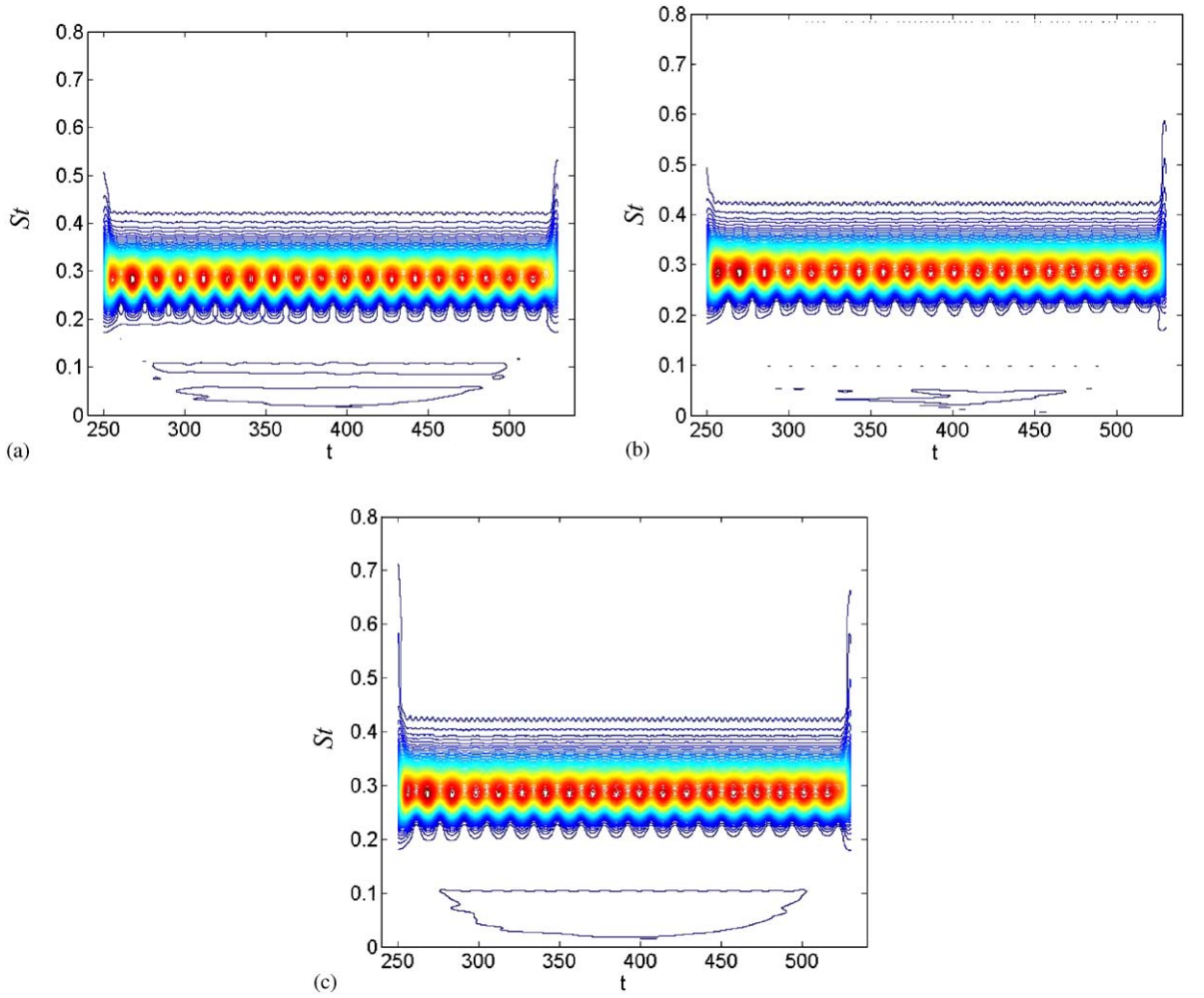


Fig. 12. Wavelet analysis of $C_D$ for (a) $Z = 9.4$, (b) $Z = 5.0$ and (c) $Z = 0.63$ at $\mathrm{Re} = 100$.

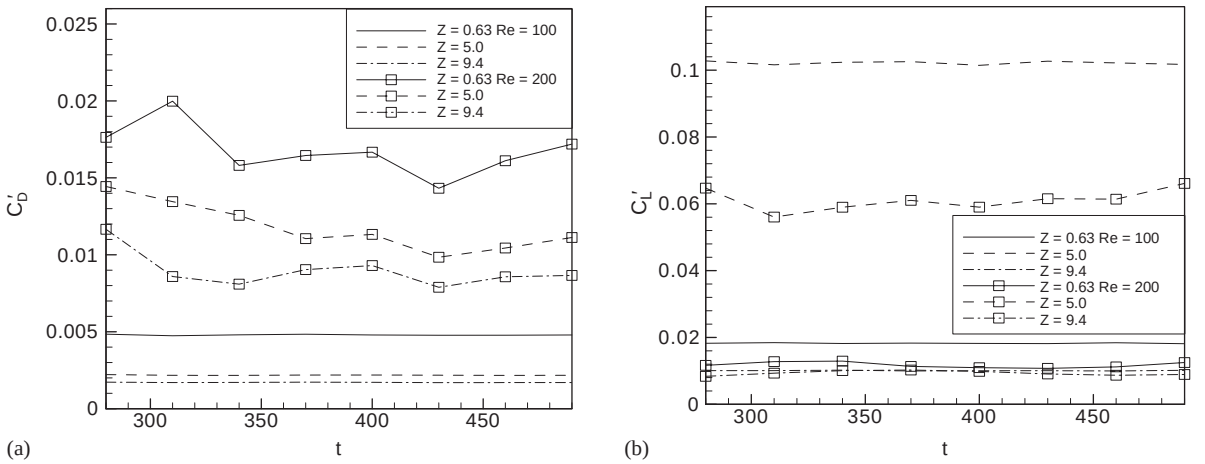


Fig. 13. RTA values of $C'_D$ and $C'_L$ at two Re and $Z = 0.63$, 5.0 and 9.4: (a) $C'_D$; (b) $C'_L$.

long before the lift does, because in the case of a 2-D cylinder in a cross-flow the only external excitation is the alternating vortex shedding from the cylinder. As a result, the lift force signal has one dominant frequency, while the drag force signal has at least two major frequencies. For the cantilevered cylinder with $L/D = 10$, a suppressed 2-D region exists. In other words, the lift force will dominate in this region and if this force is to be examined for 3-D behavior, its spatial correlation along the span should be analyzed. There is no need to examine the spatial correlation of $C_D$ $(Z,t)$ then. Since $C_L$ is a function of $Z$ and $t$, i.e. $C_L = C_L$ $(Z,t)$, spatial correlation and autocorrelation at a fixed spatial location can be calculated. Here, only the cross-correlation coefficient

$$\gamma_{ij}(\tau) = \frac{\sum_t \{[C_L(Z_i, t+\tau)][C_L(Z_j, t)]\}}{\sqrt{\sum_t [C_L(Z_i, t+\tau)]^2}\sqrt{\sum_t [C_L(Z_j, t)]^2}}, \tag{2}$$

at delay time $\tau$ between spanwise locations $i$ and $j$ is calculated. Besides the mean and r.m.s. force coefficients, $\gamma_{ij}$ for the lift force is also calculated and presented below. In addition, the spectral behavior of $C_L$ is examined in order to determined the distribution of $\mathrm{St} = \Omega_d D/U_\infty$ along the span. Here, St is to be interpreted loosely as the Strouhal number defined by the dominant frequencies ($\Omega_d$) in the spectra and not just by the shedding frequency ($\Omega_s$) alone. This analysis tends to bring out the interaction effect of the trailing and necklace vortices with the flow around the cylinder and the subsequent change of the vortex shedding frequency, if any.

The variation of $\gamma_{ij}(0)$ at zero time delay is plotted in Fig. 14. It shows the cross-correlation of $C_L$ $(Z,t)$ between $Z = 0$ and other $Z$ locations along the span. For $\mathrm{Re} = 100$, $\gamma_{ij}(0) \approx 0.95$ and this remains fairly uniform over the central region $3 < Z < 7$. Near the free end, $\gamma_{ij}(0)$ quickly drops to zero suggesting a complete 3-D behavior of $C_L$. On the other hand, near the base $\gamma_{ij}(0) \approx 0.80$, thus suggesting that $C_L$ is relatively more 2-D near the base than near the free end. As Re increases to 150, this behavior completely disappears; $\gamma_{ij}(0) \approx 0.20$ and suggests that $C_L$ is undergoing a transition to 3-D behavior. Furthermore, the relatively uniform $\gamma_{ij}(0)$ in the central region completely disappears even though $\gamma_{ij}(0) \approx 1$ at mid-span. At $\mathrm{Re} = 200$, $\gamma_{ij}(0) = 0$ at the base and becomes negative in the region $Z < 2$. This shows that the effect of the interaction with the necklace vortex gives rise to a complete 3-D behavior of $C_L$. These results are consistent with the wake flow and the force coefficients presented earlier.

The spectrum of $C_L$ is calculated using FFT and all dominant frequencies are identified for the calculation of St. Sample plots of the spectra for $\mathrm{Re} = 100$ and 200 at selected $Z$ locations are shown in Fig. 15. The spectral plots clearly show that, at midspan, there is only one dominant peak and this occurs at $\mathrm{St} = 0.145$. This value is consistent with $\mathrm{St} = 0.1476$ reported by Dauchy et al. (1997) who investigated the primary and secondary instabilities of a cylinder wake with a free end at $L/D = 10.7$ and $\mathrm{Re} = 100$. As the free end is approached, the peak at $\mathrm{St} = 0.145$ disappears but peaks occur at other locations instead. This behavior is also observed as the base is approached. In order to assess the effect of Re on the behavior of St along the span, St for $\mathrm{Re} = 100$ and 200 are calculated from the various spectral plots

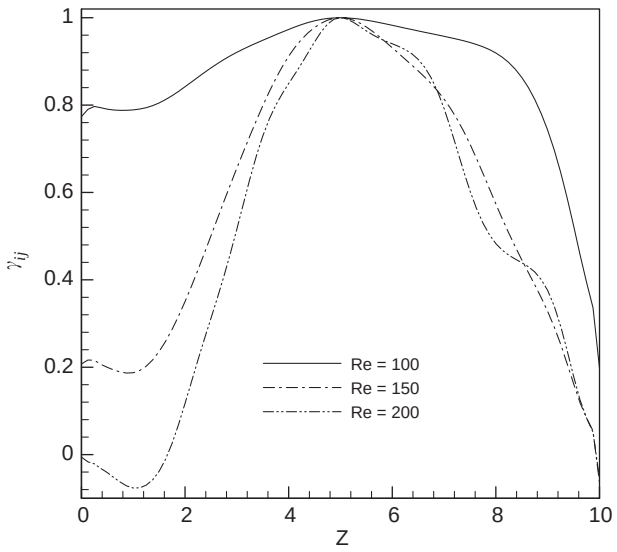


Fig. 14. Cross correlation of the lift coefficient between $Z = 0$ and other $Z$ locations.

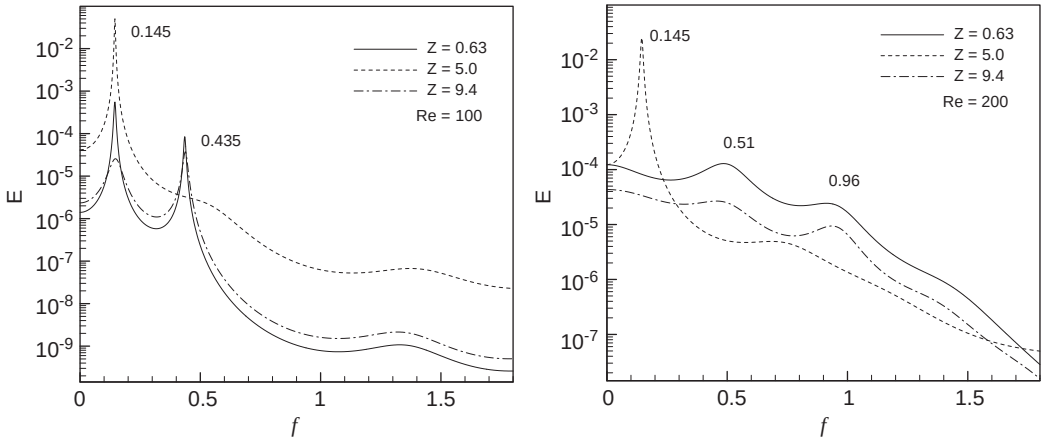


Fig. 15. Spectral analysis of $C_L$ at three $Z$ locations and two Re.

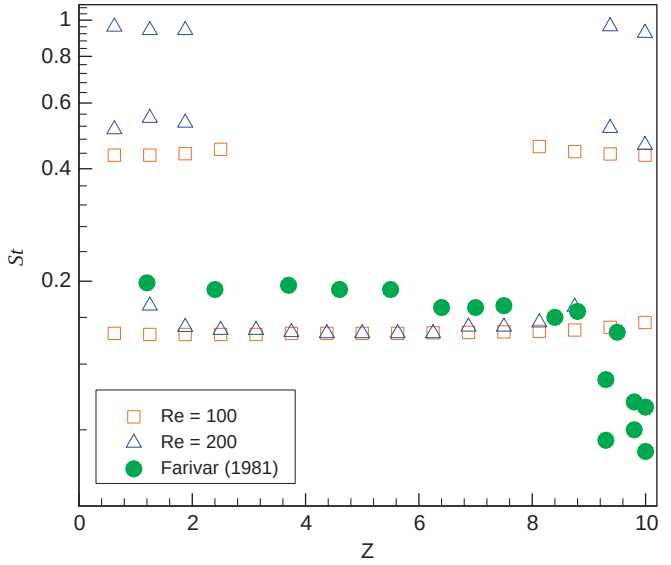


Fig. 16. Comparison of the spanwise distribution of St with data of Farivar (1981).

and shown in Fig. 16 together with the results reported by Farivar (1981) at $\mathrm{Re} = 7 \times 10^4$. Even though the Re of Farivar's experiment (1981) is much larger than the present investigation, the comparison is still meaningful because it will show the similarity of the overall trend or lack thereof for these different Re. It can be seen that at $\mathrm{Re} = 100$, $\mathrm{St} = 0.145$ is observed to extend from $Z = 0.63$ to 0.94. This result is consistent with that reported by Farivar (1981), even though his measured St is about 0.18 and there is more scatter in his measurements. Near the free end, extending from $Z = 8$ to 9.4, another $\mathrm{St} = 0.435$ is observed. This is also true near the base, where the second dominant frequency is observed to extend from $Z = 2.5$ down to $Z = 0.63$. This is the third harmonic of $\mathrm{St} = 0.145$. At $\mathrm{Re} = 200$, the region where $\mathrm{St} = 0.145$ only covers $Z = 2$ to 8. Near the free end ($Z > 9$), only $\mathrm{St} \approx 0.51$ and 0.96 are observed. Near the base ($Z < 1$), these two Strouhal numbers are also observed; again $\mathrm{St} = 0.145$ has disappeared. Unlike the region near the free end, in the region $1 < Z \leqslant 2$ three dominant frequencies are observed, including the $\mathrm{St} = 0.145$ frequency. This tends to support the suggestion that there is a fundamental difference between the interaction near the free end and that near the base. The difference could be gleaned from the $\boldsymbol{\varpi}_y$ plots shown in Fig. 5.

## 4. Conclusions

A cantilevered cylinder with $L/D = 10$ in a cross-flow at $\mathrm{Re} = 100$, 150 and 200 is simulated using the LBM method. This three-dimensional simulation leads to the following conclusions:

(i) The simulations show that for all Re investigated, there exists a suppressed 2-D region in the central portion of the finite cylinder. Near the free end, the wake flow interacts with the trailing vortex to give rise to 3-D effects. The same also happens near the base, where the interaction is between the necklace vortex and the wake flow.
(ii) The extent of this interaction is not the same near the free end and near the base. It is affected by the Reynolds number.
(iii) It is this interaction that gives rise to oblique vortex shedding along the span in the central part of the cylinder span.
(iv) As Re increases, the extent of the interaction regions increases and the suppressed 2-D region decreases. This effect is quite significant, although Re increases from 100 to 200.
(v) The unsteady forces along the span have an entire 3-D behavior with $\bar{C}_D$ increases from a low at the base to a maximum at about $Z = 1$, then drops to a plateau in the central part of the span and further increases toward the free end. This overall trend is true for all Re investigated, but the magnitude decreases significantly with Re.
(vi) The same behavior of a reduction in magnitude as Re increases is also true for $C'_L$ but not for $C'_D$. Instead, $C'_D$ increases with Re. This increase reduces the ratio $C'_L/C'_D$ as Re increases and could be interpreted as an indication of the slow disappearance of the suppressed 2-D region.
(vii) Further evidence that the unsteady forces are 3-D in nature is provided by the distribution of St along the span. Near the free end and the base, multiple St appear while the fundamental St disappears. This too is affected by Re.
(viii) All unsteady forces are stationary along the span at $\mathrm{Re} = 100$. However, as Re increases, the spanwise fluctuating drag will become more and more non-stationary. At $\mathrm{Re} = 200$, the $C_D$ time series essentially becomes non-stationary along the span. However, this non-stationary character is not reflected in the $\bar{C}_D$ behavior for all Re investigated.

## Acknowledgements

Support given by the Research Grants Council of the Government of the HKSAR under Grant Nos. PolyU5166/01E, PolyU5172/02E, PolyU5174/02E and PolyU1/02C, and by the Hong Kong Polytechnic University Central Research Grant A-PD75 is gratefully acknowledged.

## References

Baban, F., So, R.M.C., 1991a. Recirculating flow behind and unsteady forces on finite-span circular cylinders in a cross-flow. Journal of Fluids and Structures 5, 185–206.

Baban, F., So, R.M.C., 1991b. Aspect ratio effect on flow-induced forces on circular cylinders in a cross-flow. Experiments in Fluids 10, 313–321.

Baban, F., So, R.M.C., Otugen, M.V., 1989. Unsteady forces on circular cylinders in a cross-flow. Experiments in Fluids 7, 293–302.

Berger, E., Wille, R., 1972. Periodic flow phenomena. Annual Review of Fluid Mechanics 4, 312–340.

Bhatnagar, P.L., Gross, E.P., Krook, M., 1954. A model for collision processes in gases. 1, small amplitude processes in charged and neutral one-component systems. Physical Review 94, 511–525.

Bloor, S., 1964. The transition to turbulence in the wake of a circular cylinder. Journal of Fluid Mechanics 19, 290–304.

Cercignani, C., 1988. The Boltzmann Equation and its Applications. Springer, New York.

Chen, H.D., Chen, S.Y., Matthaeus, W.H., 1992. Recovery of the Navier–Stokes equations using a lattice-gas Boltzmann method. Physical Review A 45, 5339–5342.

Daubechies, I., 1990. The wavelet transform time–frequency localization and signal analysis. IEEE Transaction: Information Theory 36, 961–1004.

Dauchy, C., Dusek, J., Fraunie, P., 1997. Primary and secondary instabilities in the wake of a cylinder with free ends. Journal of Fluid Mechanics 332, 295–339.

Eisenlohr, H., Eckelmann, H., 1989. Vortex splitting and its consequences in vortex street wake of cylinder at low Reynolds numbers. Physics of Fluids A 1, 189–192.

Farivar, D., 1981. Turbulent uniform flow around cylinders a finite length. AIAA Journal 19, 275–281.
Fox, T.A., West, G.S., 1993. Fluid-induced loading of cantilevered circular cylinder in cross flow, Part I: mean loading with aspect ratio in the range 4–30. Journal of Fluids Structure 7, 1–14.
Fröhlich, J., Rodi, W., 2004. LES of the flow around a circular cylinder of finite height. International Journal of Heat and Fluid Flow 25, 537–548.
Gerich, D., Eckelmann, H., 1982. Influence of end plates and free ends on the shedding frequency of circular cylinder. Journal of Fluid Mechanics 122, 109–121.
Guo, Z., Shi, B.C., Wang, N.C., 2000. Lattice BGK model for incompressible Navier–Stokes equation. Journal of Computational Physics 165, 288–306.
He, X.Y., Luo, L.-S., 1997a. Lattice Boltzmann model for the incompressible Navier–Stokes equation. Journal of Statistical Physics 88, 927–934.
He, X.Y., Luo, L.-S., 1997b. A priori derivation of the lattice Boltzmann equation. Physical Review E 55 (Part A), R6333–R6336.
Kawamura, T., Hiwada, M., Hibino, T., Mabuchi, I., Kamuda, M., 1984. Flow around a finite circular cylinder on a flat plate. Bulletin of the JSME 27 (232), 2142–2151.
Köng, M., Eisenlohr, H., Eckelmann, H., 1990. The fine structure in the S–Re relationship of the laminar wake of a circular cylinder. Physics of Fluids A 2, 1607–1611.
Lam, K., Wang, F.H., So, R.M.C., 2004. Three-dimensional nature of vortices in the near wake of a wavy cylinder. Journal of Fluids and Structures 19, 815–833.
Martinuzzi, R., Tropea, C., 1993. The flow around surface-mounted, prismatic obstacles placed in a fully developed channel flow. Journal of Fluids Engineering 115, 85–92.
Matsumoto, M., 1999. Vortex shedding of bluff bodies: a review. Journal of Fluids and Structures 13, 791–811.
McNamara, G.R., Zanetti, G., 1988. Use of the Boltzmann equation to simulate lattice-gas automata. Physical Review Letters 61, 2332–2335.
Norberg, C., 2003. Fluctuating lift on a circular cylinder: review and new measurements. Journal of Fluids and Structures 17, 57–96.
Okamoto, S., Sunabashiri, Y., 1992. Vortex shedding from a circular cylinder of finite length placed on a ground plane. ASME Journal of Fluids Engineering 114, 512–521.
Okamoto, T., Yagita, M., 1973. Experimental investigation on the flow past a circular cylinder of finite length placed normal to the plane surface in a uniform stream. Bulletin of the JSME 16, 805–814.
Park, C.-W., Lee, S.-J., 2000. Free end effects on the near wake flow structure behind a finite circular cylinder. Journal of Wind Engineering and Industrial Aerodynamics 88, 231–246.
Park, C.-W., Lee, S.-J., 2004. Effects of free-end corner shape on flow structure around a finite cylinder. Journal of Fluids and Structures 19, 141–158.
Richter, A., Naudascher, E., 1976. Fluctuating forces on a rigid circular cylinder in confined flow. Journal of Fluid Mechanics 78, 561–576.
Roshko, A., 1993. Perspectives on bluff body aerodynamics. Journal of Wind Engineering and Industrial Aerodynamics 49, 79–100.
Sakamoto, H., Arie, M., 1983. Vortex shedding from a rectangular prism and a circular cylinder placed vertically in a turbulent boundary layer. ASME Journal of Fluid Mechanics 126, 147–165.
Sakamoto, H., Oiwake, S., 1984. Fluctuating forces on a rectangular prism and a circular cylinder placed vertically in a turbulent boundary layer. ASME Journal of Fluids Engineering 106, 160–166.
Sarode, R.S., Gai, S.L., Ramesh, C.K., 1981. Flow around circular- and square-section models of finite height in a turbulent shear flow. Journal of Wind Engineering of Industrial Aerodynamics 8, 223–230.
Sin, V.K., So, R.M.C., 1987. Local force measurement on finite span cylinders in a cross flow. ASME Journal of Fluids Engineering 109, 136–143.
Slaouti, A., Gerrard, J.H., 1981. An experimental investigation of the end effects on the wake of a circular cylinder towed through water at low Reynolds numbers. Journal of Fluid Mechanics 112, 297–314.
So, R.M.C., Savkar, S.D., 1981. Buffeting forces on rigid circular cylinders in cross flows. Journal of Fluid Mechanics 105, 397–425.
So, R.M.C., Liu, Y., Cui, Z.X., Zhang, C.H., Wang, X.Q., 2005. Three-dimensional wake effects on the flow-induced forces. Journal of Fluids and Structures 20, 373–402.
Stager, R., Eckelmann, H., 1991. The effects of endplates on the shedding frequency of circular cylinders in the irregular range. Physics of Fluids A 3, 2116–2121.
Szepessy, S., Bearman, P.W., 1992. Aspect ratio and end plate effects on vortex shedding from a circular cylinder. Journal of Fluid Mechanics 234, 191–217.
Williamson, C.H.K., 1988. The existence of two stages in the transition to three-dimensionality of a cylinder wake. Physics of Fluids 31, 3165–3168.
Williamson, C.H.K., 1989. Oblique and parallel mode of vortex shedding in the wake of a cylinder at low Reynolds numbers. Journal of Fluid Mechanics 206, 579–627.
Williamson, C.H.K., 1992. The natural and forced formation of spot-like vortex dislocations in the transition of a wake. Journal of Fluid Mechanics 243, 393–441.

Williamson, C.H.K., 1996a. Vortex dynamics in the cylinder wake. Annual Review of Fluid Mechanics 28, 477–539.
Williamson, C.H.K., 1996b. Three-dimensional wake transition. Journal of Fluid Mechanics 328, 345–407.
Yu, D.Z., Mei, R.W., Shyy, W., 2002. A multi-block lattice Boltzmann method for viscous fluid flows. International Journal for Numerical Methods in Fluids 39, 99–120.
Zdravkovich, M.M., 1997. Flow around circular cylinders. Fundamentals, vol 1. Oxford University Press, Oxford.
Zhang, J., Dalton, C., 1998. A three-dimensional simulation of a steady approach flow past a circular cylinder at low Reynolds number. International Journal of Numerical Methods in Fluids 26, 1003–1022.